Multichannel nonreciprocal amplifications using cesium vapor

Yao-Dong Hu[1] and Guo-Qiang Zhang[1,2]
[1]*Interdisciplinary Center of Quantum Information, State Key Laboratory of Modern Optical Instrumentation, and Zhejiang Province Key Laboratory of Quantum Technology and Device, School of Physics, Zhejiang University, Hangzhou 310027, China*
[2]*School of Physics, Hangzhou Normal University, Hangzhou, Zhejiang 311121, China*

(Received 13 December 2022; revised 4 April 2023; accepted 17 May 2023; published 31 May 2023)

Multichannel synchronous amplifications are an inevitable key problem in quantum communication process, which can broaden the bandwidth of transmitted signals and establish correlation among different optical channels. Here we study a nonreciprocal system with four concurrent amplification channels using hot cesium atoms, both theoretically and experimentally. For the forward probe field, the double–electromagnetically induced transparency structure is formed and the phase-matching condition of the multiwave mixing process is satisfied, which are both destroyed when the probe field is reversed. In addition, the four-channel nonreciprocal amplifications are formed in the Zeeman sublevels of the system with special selection of light field polarization, which will also dramatically enhance the signal-to-noise ratio by suppressing the spontaneous emission noise of the system. In our experiment, the quadruple nonreciprocal amplifications are achieved with the maximum forward gain reaching 30 dB and the reverse suppression reaching–23 dB. The gain adjustability allows the construction of a gain-loss balanced system, providing a scheme for an atomic system to engineer a parity-time-symmetric (or -antisymmetric) structure.

DOI: 10.1103/PhysRevA.107.053716

I. INTRODUCTION

Nonreciprocal devices [1–6] exhibit anisotropic transmission and isolation properties by breaking Lorentz reciprocity [7], which always holds true in nonmagnetic linear media guaranteed by Maxwell equations. These devices have boosted the development of communication networks due to their ability of protecting coherent information processing from noise and backscattering. Common schemes related to nonreciprocity are based on magneto-optical materials that provide asymmetrical permittivity tensors [8]. As the demand for on-chip integration grows, numerous alternative linear schemes have been proposed without a reliance on magneto-optical effects, including indirect interband photonic transitions [9,10], spatiotemporal modulation [11–15], optomechanical interaction [16–19], etc.

Unlike linear schemes, strong nonlinear interactions between photons are beneficial to the observation of quantum effects in optics and the compensation for the inevitable loss in the transmission process. Studies that combine nonlinearity and nonreciprocity include second harmonic generation in asymmetric waveguides [20], metastructure [21–23], and photonic quasicrystals [24,25]. Also, atomic systems, which have the advantage of high tunability and strong quantum interference, are an indispensable implementation to achieve nonreciprocal amplifications, based on Kerr optical nonlinearities [5,26–29], multiwave mixing [30] and nonlinear Raman interaction [31]. However, these pioneering nonreciprocal atomic systems with amplification normally contain just one signal channel.

Since multichannel interaction in atomic systems is crucial for long-distance quantum communication [32], it is of great significance to develop multichannel nonreciprocal systems. Particularly, the associated photon pairs generated using spontaneous parametric down-conversion processes [33] and spontaneous four-wave mixing processes [34] provide useful bipartite entanglement in, e.g., energy time [35–38], polarization [39], and orbital angular momentum [40,41]. Thus it is worthwhile to construct multiple associated channels to realize nonreciprocal gains synchronously.

In this work we provide an all-optical nonreciprocal system with multiple amplification channels in cesium (Cs) atoms by breaking both the time-reversal symmetry [1] and the spacial inversion symmetry [42]. The technique we utilize here is electromagnetically induced transparency (EIT), an effective method in atomic systems to reduce the absorption of the probe field, which has been integrated onto chips [43–47]. The requirement for the EIT effect is the two-photon resonance condition, which is irrelevant with the propagation directions of the fields in the absence of Doppler effect. This reciprocal nature of EIT will be broken once we consider the inevitable microscopic Doppler effect in warm atoms, which will shift the frequencies of the fields. The frequency shifts are related to the propagation directions of the fields, which means that it will be different when the probe field propagates in the opposite direction and thus breaks the time-reversal symmetry. As for the spatial inversion symmetry, the generation and amplification of the weak fields are all based on the multiwave mixing processes, where the phase-matching condition is always indispensable. This condition is a request for the spatial relationship of the wave vectors, which is related to the momentum conservation. That is to say, once we input a probe field from the opposite direction with the directions of other fields unchanged, this condition will be also broken, leading

to the breaking of the spatial inversion symmetry. These two breakings indicate that the transparency windows and nonlinear amplifications are nonreciprocal. To our knowledge, this study is the first realization of multichannel nonreciprocal amplifications, which has potential applications in, e.g., preparing the nonreciprocal entangled (superentangled) photon pairs [40].

The paper is organized as follows. In Sec. II we introduce the model of the multichannel nonreciprocal amplifications. The experimental results are shown in Sec. III, and discussions and conclusions are given in Sec. IV. Also, some theoretical results used for explaining the experimental observations are given in the Appendix.

II. MODEL

A. Physical mechanism of the multichannel amplifications

The development of double-EIT [48] and even double-double EIT [49] provides us the opportunity to achieve multichannel systems with transparency windows. Moreover, the degenerated Zeeman sublevels of Cs atoms [50], on the one hand, offer us a subtle platform to construct multi-tripod-type energy-level structures with only one or two coupling fields but on the other, suffer from the complexity of its large numbers of the sublevels. By skillful design of the field polarization, we manage to overcome this weakness and consequently achieve a nonreciprocal optical system with four amplification channels in the Zeeman sublevels of Cs atoms.

As schematically shown in Fig. 1(a), the Cs atomic vapor cell is embedded in a magnetic shield barrel, where two π-polarized coupling fields [coupling field 1 (blue arrow) and coupling field 2 (green arrow)] and a σ^+- and σ^--polarized probe field (red arrow) nearly colinearly pass through the vapor cell. Here we only consider the two ground states ($6^2S_{1/2}$, $F_g = 3$, $F_g = 4$) and one excited state ($6^2P_{1/2}$, $F_e = 4$) in the D1 line of Cs atoms [cf. Figs. 1(b) and 1(c)], where $F_{g,e}$ is the total angular momentum, and the frequency splitting between the two hyperfine ground energy levels is $\delta/2\pi = 9.2$ GHz. For convenience, we denote these Zeeman sublevels by $|a_{m_F}\rangle$ ($6^2S_{1/2}, F_g = 3$), $|b_{m_F}\rangle$ ($6^2S_{1/2}, F_g = 4$) and $|c_{m_F}\rangle$ ($6^2P_{1/2}, F_e = 4$), with m_F ($= -F_{g,e}, -F_{g,e}+1, \ldots, F_{g,e}-1, F_{g,e}$) being the projection of $F_{g,e}$ along the y axis. Since the geomagnetic field is screened, the Zeeman sublevels $|a_{m_F}\rangle$ ($|b_{m_F}\rangle$, $|c_{m_F}\rangle$) are degenerate [51]. The coupling field 1 with frequency ω_1 (blue arrow) is set to be in resonance with the transition $|c_{m_F}\rangle \to |a_{m_F}\rangle$, while the coupling field 2 with frequency ω_2 (green arrow) is blue detuned from the transition $|c_{m_F}\rangle \to |b_{m_F}\rangle$ by $\Delta/2\pi \approx 40$ MHz. The frequency ω_p of the probe laser is scanned around the transition frequency between the two states $|c_{m_F}\rangle$ and $|b_{m_F}\rangle$.

In the steady state, due to the forbidden nature of the transition between $|b_0\rangle$ and $|c_0\rangle$, almost all atoms are in the state $|b_0\rangle$. This special population case as well as the symmetric energy-level structure of Cs atoms allow us to draw a simplified picture [see Fig. 1(c) and Appendix B for more details]. As shown in Fig. 2(a), the injected probe field (red solid arrow) generates the conjugated field (with frequency $\omega_{conj} = \omega_p + \delta - \Delta$; blue dotted arrow) via interaction with the two

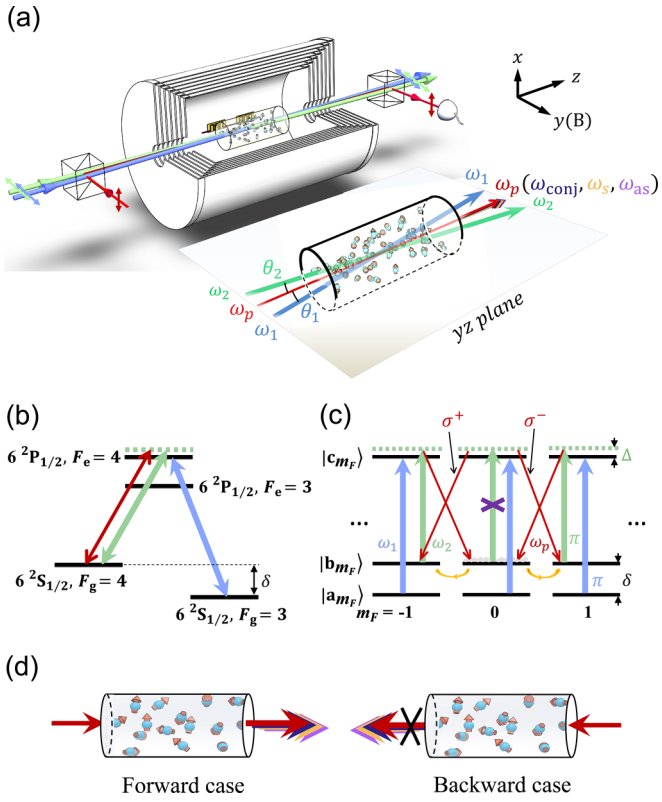

FIG. 1. Illustration of the principles of nonreciprocal multichannel synchronous amplification system based on a Cs atomic vapor cell. (a) Experimental apparatus. Blue and green arrows: (π-polarized) coupling fields 1 and 2; Red arrow: (σ^+- and σ^--polarized with equal components) probe field. $\updownarrow$ denotes the linear polarization. The probe field and coupling fields are mixed by a polarizing beam splitter before entering into the Cs atomic vapor cell and then separated by another polarizing beam splitter after exporting from the Cs atomic vapor cell. In addition, the spatial distribution of these input fields is illustrated, where the relative angles between each coupling field and the probe field are chosen as $\theta_1 = \theta_2 = 3.45$ mrad (see Appendix A). (b) The hyperfine energy levels in the Cs D1 line [50]. Note that the energy level $6^2P_{1/2}$, $F_e = 3$ is decoupled from the two coupling fields and the probe field. (c) The diagram of Zeeman sublevels. (d) The conceptual view of the nonreciprocal behavior in the atomic system with probe field injected from two directions.

coupling fields, where the four-wave mixing (FWM) process, i.e., $|b_1\rangle \to |c_1\rangle \to |b_0\rangle \to |c_0\rangle \to |b_1\rangle$, amplifies both the probe and conjugated fields. Then the amplified probe field will repump the atoms from $|b_0\rangle$ to $|c_1\rangle$, which leads to a six-wave mixing (SWM) process, i.e., $|b_1\rangle \to |c_1\rangle \to |b_0\rangle \to |c_1\rangle \to |a_0\rangle \to |c_0\rangle \to |b_1\rangle$ [see Fig. 2(b)], where the Stokes (with frequency $\omega_s = \omega_p - \Delta$; yellow dotted arrow) and the anti-Stokes (with frequency $\omega_{as} = \omega_p + \delta$; purple dotted arrow) fields are generated. Furthermore, the FWM process in the SWM process [i.e., $|b_1\rangle \to |c_1\rangle \to |a_0\rangle \to |c_0\rangle \to |b_1\rangle$; see Fig. 2(c)] also amplifies the two generated fields. The two FWM processes form the two double-EIT (DEIT) structures [48,49], where one DEIT structure consists of the states $|b_1\rangle$, $|c_1\rangle$, $|a_0\rangle$, and $|b_0\rangle$, and the other is formed by $|a_1\rangle$, $|c_1\rangle$, $|a_0\rangle$, and $|b_0\rangle$ [cf. Fig. 2(d)]. This provides the four corresponding transparency windows for the amplified probe, conjugated, Stokes, and anti-Stokes fields.

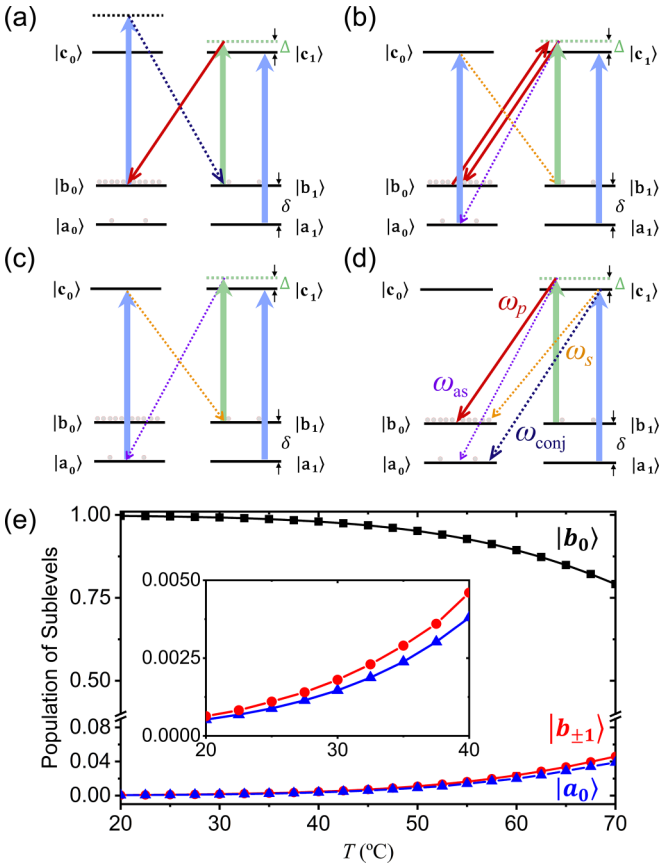

FIG. 2. (a)–(d) Simplified level diagrams with the most populated sublevels. (a) The generation and amplification process of the probe and conjugated fields by a FWM process. (b) A mediated SWM process that connects the probe and Stokes/anti-Stokes fields. (c) The FWM process in the SWM process will further amplify the Stokes and anti-Stokes fields. (d) The injected probe field and the generated conjugated, Stokes and anti-Stokes fields, are all in the transparency windows of two DEIT structures. (e) Population of the sublevels, $|b_0\rangle$, $|b_{\pm1}\rangle$, and $|a_0\rangle$, vs the temperature T of the atomic vapor cell, which are calculated using Eqs. (C5)–(C9) in Appendix C. Inset: the enlarged view of the population of the sublevel $|a_0\rangle$ and $|b_{\pm1}\rangle$. The parameters used in the simulation are $\gamma_{c_{0,1}}/2\pi = 4.6\,\text{MHz}$, $\Omega_1 = 8.7\gamma_{c_0}$, $\Omega_2 = 14\gamma_{c_0}$, $\Delta_1 = 0$, $\Delta_2/2\pi = 40\,\text{MHz}$, and $\gamma_{a_0,a_1}/2\pi = \gamma_{b_0,b_1}/2\pi = 9\kappa n(T)$, where $\kappa \approx 6\times10^{-10}\ \text{cm}^3\,\text{s}^{-1}$, and the collisional dephasing effect has been neglected [51]. The atomic density is given by $n(T) = P_v/k_BT$, with the Boltzmann constant k_B and the pressure $P_v(T) = 10^{7.046-3830/T}$ [50].

In the above processes, almost all Cs atoms in the sublevel $|b_0\rangle$ are forbidden to interact with the coupling fields due to the selection rules, leading to weak spontaneous emission noises. On the other hand, other sublevels have so few Cs atoms that the corresponding noises are also weak, despite that they are coupled to near-resonant coupling fields. Thus the noises are tremendously suppressed in our system, and the signal-to-noise ratio of the multichannel nonreciprocal amplifications can be significantly improved [52].

B. Theoretical results

In this section we derive the susceptibilities χ_1 and χ_2 of the weak fields, where χ_1 contains ω_p and ω_{conj} [cf. Fig. 2(a)], while χ_2 contains ω_s and ω_{as} [cf. Fig. 2(c)]. In the interaction picture the Hamiltonian for the FWM processes in Figs. 2(a) and 2(c) are [53–57]

$$H_{\text{int}}^{(1)} = \tfrac{1}{2}\big[\Omega_1 e^{i(k_1 z-\Delta_1 t)}\big(\sigma_{c_1a_1}+\sigma_{c_0b_0}\big)+\Omega_2 e^{i(k_2 z-\Delta_2 t)}\sigma_{c_1b_1} + \Omega_p e^{i(k_p z-\Delta_p t)}\sigma_{c_1b_0}+\Omega_{\text{conj}} e^{i(k_{\text{conj}} z-\Delta_{\text{conj}} t)}\sigma_{c_0b_1}+\text{H.c.}\big] \tag{1}$$

and

$$H_{\text{int}}^{(2)} = \tfrac{1}{2}\big[\Omega_1 e^{i(k_1 z-\Delta_1 t)}\big(\sigma_{c_1a_1}+\sigma_{c_0a_0}\big)+\Omega_2 e^{i(k_2 z-\Delta_2 t)}\sigma_{c_1b_1} + \Omega_{\text{as}} e^{i(k_{\text{as}} z-\Delta_{\text{as}} t)}\sigma_{c_1a_0}+\Omega_s e^{i(k_s z-\Delta_s t)}\sigma_{c_0b_1}+\text{H.c.}\big], \tag{2}$$

respectively, where ω_x is the eigenenergy of state $|x\rangle$, $k_{1,2}$ and $\Omega_{1,2}$ ($k_{p,\text{conj},s,\text{as}}$ and $\Omega_{p,\text{conj},s,\text{as}}$) stand for the wave vectors and the Rabi frequencies of the coupling fields (weak fields), and $\sigma_{xy} = |x\rangle\langle y|$ ($\{x,y\} = \{a_{m_F}, b_{m_F}, c_{m_F}\}$, $x \neq y$) denote the atomic transition operators with transition frequency $\omega_{xy} = \omega_x - \omega_y$. When we consider the Doppler frequency shifts induced by atomic thermal motion, the frequency detunings can be expressed as $\Delta_1 = (\omega_1 + k_1 v) - \omega_{c_1a_1}$, $\Delta_2 = (\omega_2 + k_2 v) - \omega_{c_1b_1}$, $\Delta_{p,s} = (\omega_{p,s} \pm k_{p,s} v) - \omega_{c_1b_0}$, and $\Delta_{\text{conj,as}} = (\omega_{\text{conj,as}} \pm k_{\text{conj,as}} v) - \omega_{c_1a_0}$, where $+k_{p,s}v$ and $+k_{\text{conj,as}}v$ ($-k_{p,s}v$ and $-k_{\text{conj,as}}v$) correspond to the forward (backward) probe field, and v is the velocity of Cs atoms.

With the Hamiltonians in Eqs. (1) and (2), we can obtain the susceptibility χ of the weak fields by solving the master equations (see Appendix D) [48,49,51]:

$$\chi = \chi_1 + \chi_2, \tag{3}$$

$$\chi_1 = \int_{-\infty}^{\infty} \frac{iN|d_{c_1b_0}|^2}{\epsilon_0\Omega_p}\big(C_{\text{DEIT}}^{(1)} + C_{\text{SRS}}^{(1)} + C_{\text{FWM}}^{(1)} e^{i\Delta k_{\text{FWM}}^{(1)} z}\big) f(v)dv, \tag{4}$$

$$\chi_2 = \int_{-\infty}^{\infty} \frac{iN|d_{c_1a_0}|^2}{\epsilon_0\Omega_{\text{as}}}\big(C_{\text{DEIT}}^{(2)} + C_{\text{SRS}}^{(2)} + C_{\text{FWM}}^{(2)} e^{i\Delta k_{\text{FWM}}^{(2)} z}\big) f(v)dv, \tag{5}$$

where N stands for the atomic density, $d_{c_1b_0} = \langle c_1|\mathbf{d}|b_0\rangle$ and $d_{c_1a_0} = \langle c_1|\mathbf{d}|a_0\rangle$ are the corresponding matric elements of the dipole moment $\mathbf{d}$ of Cs atoms, ϵ_0 denotes the permittivity of free space, and $f(v) = \exp(-v^2/u^2)/u\sqrt{\pi}$ is the Maxwell velocity distribution, with $u = \sqrt{2k_B T_{\text{at}}/m}$ being the most probable velocity, k_B the Boltzmann constant, T_{at} the temperature of atoms, and m the mass of a Cs atom. The coefficients $C_{\text{DEIT}}^{(1,2)}$, $C_{\text{SRS}}^{(1,2)}$, and $C_{\text{FWM}}^{(1,2)}$ given in Appendix D are functions of the two-photon detunings $\Delta_{\text{p2}} = (\omega_p \pm k_p v) - (\omega_2 + k_2 v)$, $\Delta_{\text{conj1}} = (\omega_{\text{conj}} \pm k_{\text{conj}} v) - (\omega_1 + k_1 v)$, $\Delta_{\text{as2}} = (\omega_{\text{as}} \pm k_{\text{as}} v) - (\omega_2 + \delta + k_2 v)$, and $\Delta_{\text{s1}} = (\omega_s + \delta \pm k_s v) - (\omega_1 + k_1 v)$, while $\Delta k_{\text{FWM}}^{(1)} = k_1 + k_2 \mp k_p \mp k_{\text{conj}}$ and $\Delta k_{\text{FWM}}^{(2)} = k_1 + k_2 \mp k_{\text{as}} \mp k_s$ denote the momentum-mismatching of the two FWM processes in Figs. 2(a) and 2(c). For simplicity, we assume $k_1 \approx k_2 \approx k_p \approx k_{\text{conj}} \approx k_{\text{as}} \approx k_s$ in the following analysis.

To quantitatively describe the four-channel nonreciprocal amplifications, we define the gain

$$g \equiv \frac{P_p}{P_0} = \exp[-kL\text{Im}(\chi)], \tag{6}$$

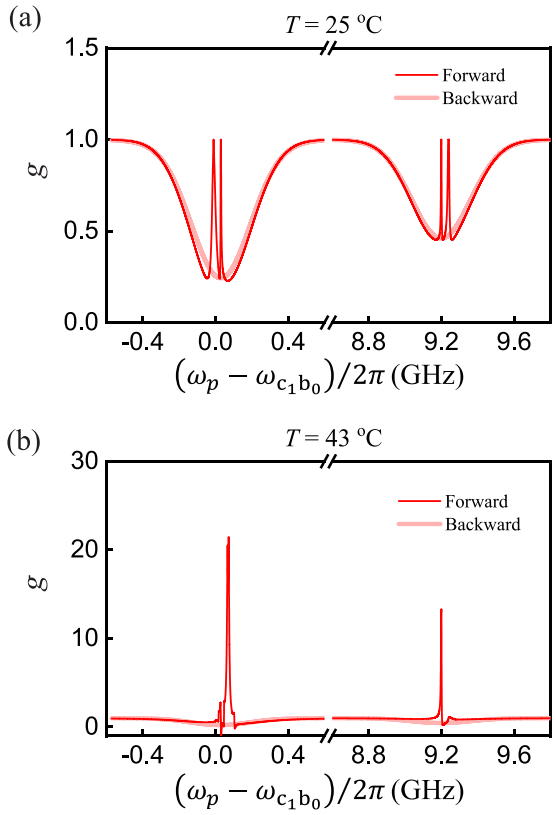

FIG. 3. Theoretical simulations of the gain spectra at (a) room temperature $T = 25$ °C and (b) warm temperature $T = 43$ °C using Eq. (6), where the ToP rate, $\gamma'_{ab} = \kappa n(T)$, is $\gamma'_{ab}/2\pi = 30$ Hz in (a) and $\gamma'_{ab}/2\pi = 166$ Hz in (b), respectively. Other parameters are chosen to be $\gamma_{c_0}/2\pi = \gamma_{c_1}/2\pi = 4.6$ MHz, $\gamma'_{ba} = 9\gamma'_{ab}/7$, $\Omega_1 = 8.7\gamma_{c_0}$, $\Omega_2 = 14\gamma_{c_0}$, $\Omega_p = \Omega_{conj} = \Omega_s = \Omega_{as} = 0.2\gamma_{c_0}$, $\Delta_1 = 0$, and $\Delta_2/2\pi = 40$ MHz.

where P_0 (P_p) is the input (output) power of the weak field, and L is the length of the vapor cell. In Fig. 3 we plot the gain g versus the detunings $\Delta_p/2\pi$ of the probe field at different temperatures. At $T = 25$ °C, the Doppler-broadened absorption background is clearly visible for both the forward and backward cases, while the four transparency windows only occur in the forward case [see Fig. 3(a)]. This nonreciprocity results from the fact that the two-photon resonance conditions in the EIT structures and the momentum conservation conditions in the FWM processes are broken in the backward case. The two-photon resonance $\Delta_{p2} = \Delta_{conj1} = \Delta_{as2} = \Delta_{s1} = 0$ is essential in the EIT structures. When the system is Doppler-free for the forward probe field (i.e., $\Delta_{p2} = \omega_p - \omega_2$, $\Delta_{conj1} = \omega_{conj} - \omega_1$, $\Delta_{as2} = \omega_{as} - \omega_2 + \delta$, and $\Delta_{s1} = \omega_s + \delta - \omega_1$), the two-photon detunings, Δ_{p2}, Δ_{conj1}, Δ_{as2}, and Δ_{s1}, can be tuned to zero by setting $\omega_p = \omega_2$, $\omega_{conj} = \omega_1$, $\omega_{as} = \omega_2 + \delta$, and $\omega_s + \delta = \omega_1$. Then the absorption of the probe field can be totally eliminated due to the destructive quantum interference between the excitation pathways [43]. When the probe and coupling fields have opposite directions, it is difficult to satisfy the two-photon resonant conditions, because the Cs atoms have different velocities v. Thus the EIT effect will be destroyed. Moreover, for the momentum conservation $\Delta k^{(1)}_{FWM} = k_1 + k_2 - k_p - k_{conj} = 0$ and $\Delta k^{(2)}_{FWM} = k_1 + k_2 - k_{as} - k_s = 0$ in the forward case, it is also violated for the backward case, i.e., $\Delta k^{(1)}_{FWM} = k_1 + k_2 + k_p + k_{conj} \neq 0$ and $\Delta k^{(2)}_{FWM} = k_1 + k_2 + k_{as} + k_s \neq 0$.

When increasing the temperature, e.g., from $T = 25$ °C to $T = 43$ °C (related to the steady-state population of Cs atoms), the four transparency windows become four giant gain peaks in the forward case and there are some sideband peaks due to the Autler-Townes effect [58] [cf. Figs. 3(a) and 3(b)]. For the low temperature (corresponding to low population of Cs atoms in $|b_{\pm 1}\rangle$ and $|a_0\rangle$), the FWM processes are very weak, and there are only four-channel transparencies without amplifications. When increasing the temperature, the spin-exchange collisions among Cs atoms will transfer the population of hyperfine ground levels [51]. This gives rise to the decrease of the population in $|b_0\rangle$ while increasing the population in $|b_{\pm 1}\rangle$ and $|a_0\rangle$ [see Fig. 2(e)]. It strengthens the FWM and SWM processes for realizing the four-channel amplifications.

III. EXPERIMENTAL RESULTS

Experimentally, we measure the transmission and amplification properties of the scanned probe field in a Cs atomic vapor cell and explain the experimental results with our theoretical model. Here the powers of the two coupling fields 1 and 2 and the probe field are tuned to $P_1 = 128$ mW, $P_2 = 147$ mW, and $P_p = 4$ μW, and the beam diameters are $d_1 = 0.12$ cm, $d_2 = 0.08$ cm, and $d_p = 0.03$ cm, respectively. Correspondingly, the Rabi frequency Ω_j ($j = 1, 2, p$) is given by $\Omega_j = \alpha\gamma_{c_0}\sqrt{(4P_j/\pi d_j^2)/2I_{sat}}$ [51], where α denotes the C-G coefficient, γ_{c_0} is the decay rate of excited state $|c_0\rangle$, and $I_{sat} = 2.5$ mW/cm^2 is the saturated intensity [50]. To distinguish the outgoing coupling fields and the four outgoing weak fields, the relative angles between each coupling field and the probe field are chosen as $\theta_1 = \theta_2 = 3.45$ mrad, which may result in both a slight shift of the locations of the four giant gain peaks and a slight decrease of the amplification effect (see Appendix A). In Figs. 4(a) and 5(a), we show the measured gain g versus the detuning $\Delta_p/2\pi$ at $T = 25$ °C and $T = 55$ °C, respectively. At the low temperature, e.g., $T = 25$ °C, there are four transparency windows without amplifications in the Doppler-broadened absorption background for the forward case, while the four transparency windows disappear when the probe field is backward [see Fig. 4(a)]. These experimental results match well with the theoretical predictions, cf. Figs. 4(b)–4(e). Note that there are two additional Doppler-broadened absorption backgrounds around $\Delta_p/2\pi \approx -1.4$ and 8.1 GHz [see Fig. 4(a)] which result from the resonant frequencies of the transitions $F_g = 4 \rightarrow F_e = 3$ and $F_g = 3 \rightarrow F_e = 3$ [cf. Fig. 1(b)]. Because the unwanted excited state $F_e = 3$ is decoupled from the coupling fields due to large frequency detunings between them, the EIT does not exist in the two additional Doppler-broadened absorption backgrounds. In addition, the measured Doppler broadened absorption background near $\Delta_p/2\pi = 9.2$ GHz, corresponding to the resonant frequency of the transition $F_g = 3 \rightarrow F_e = 4$ [Fig. 4(c)], is sightly different from the simulation results [Fig. 4(e)]. In the experiment, the Cs atoms are excited by the strong coupling field 1, and the number of Cs atoms in

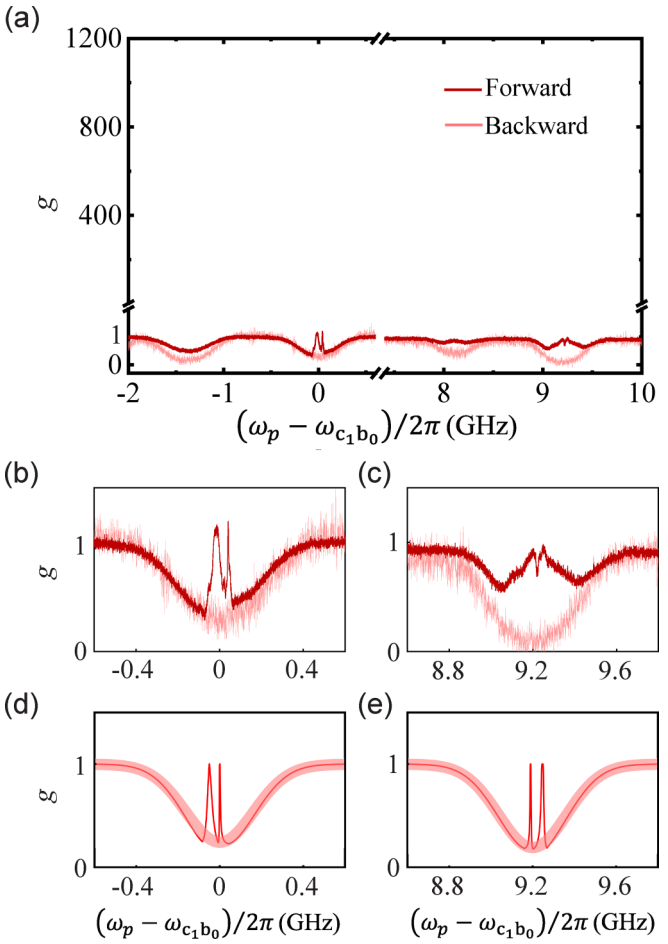

FIG. 4. (a) The measured gain g at the room temperature $T = 25\ ^\circ$C, where each gain value is obtained by averaging 20 sets of measurement data, which are measured under the same experimental conditions. Here, the gain values of the Stokes, probe, conjugate, and anti-Stokes fields are 1.12, 1.19, 0.93, and 0.95, respectively. (b) and (c) The enlarged view of the measured gain g around $\Delta_p \approx 0$ and $\Delta_p/2\pi \approx 9.2$ GHz, while the corresponding theoretical results, obtained using Eq. (6) with the ToP rate $\gamma'_{ab}/2\pi = 30$ Hz, are shown in (d) and (e). The dark red (pale red) curves in (a)–(e) correspond to the forward (backward) probe field. The parameters used in the theoretical simulation are the same as in Fig. 3.

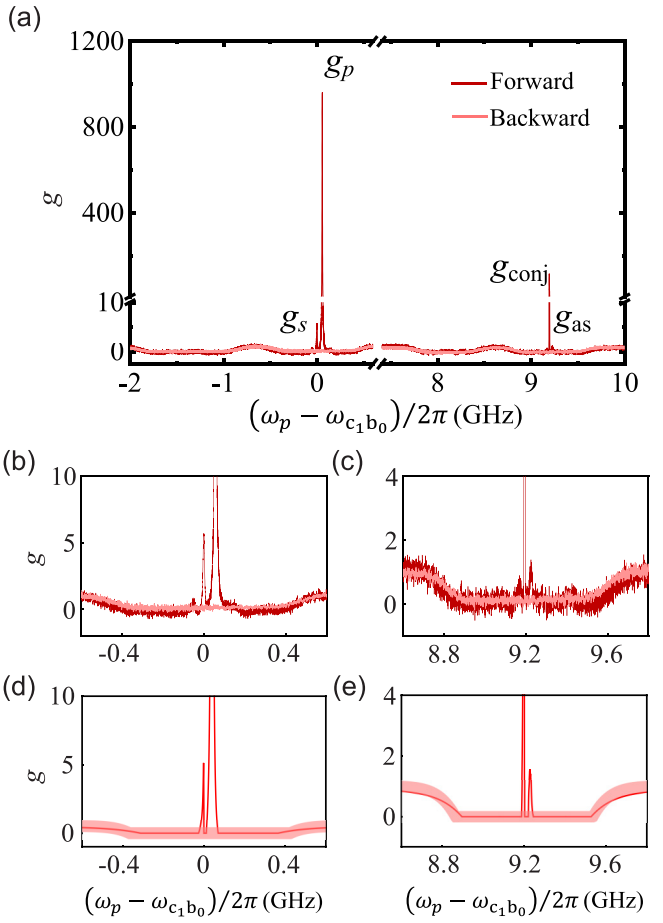

FIG. 5. (a) The measured gain g at the warm temperature $T = 55\ ^\circ$C, where each gain value is obtained by averaging 20 sets of measurement data, which are measured under the same experimental conditions. Here, the gain values of the Stokes, probe, conjugate, and anti-Stokes fields are 5.8, 962, 116, and 1.4, respectively. (b) and (c) The enlarged view of the measured gain g around $\Delta_p \approx 0$ and $\Delta_p/2\pi \approx 9.2$ GHz, while the corresponding theoretical results, obtained using Eq. (6) with the ToP rate $\gamma'_{ab}/2\pi = 505$ Hz, are shown in (d) and (e). The dark red (pale red) curves in (a)–(e) correspond to the forward (backward) probe field. The parameters used in the theoretical simulation are the same as in Fig. 3.

the ground state $|a_0\rangle$ is small. The result is that the absorption of the probe field is suppressed. In contrast, in the theoretical model we assume that there are always sufficient Cs atoms in the ground state $|a_0\rangle$, which means that the probe field can be always absorbed completely. Furthermore, when we warm up the vapor cell up to 55 °C, the four giant gain peaks occur in the forward case but do not occur in the backward case, as shown in Fig. 5(a), which is due to the population transfer in the ground states with increasing temperature. With the temperature increasing, the effect of the thermal motion of Cs atoms becomes more significant and the Doppler-broaden absorption backgrounds are broadened [cf. Figs. 4(b) and 5(b); Figs. 4(c) and 5(c)]. Besides the four giant gain peaks, there are also some small peaks at, e.g., $\Delta_p/2\pi = -0.03$ and 9.17 GHz, in the forward case [see Figs. 5(b) and 5(c)]. They may result from other multiwave mixing processes (cf. Appendix B). Here the maximum forward gain reaches $g_p = 30$ dB and the reverse suppression reaches $g_p = -23$ dB. The simulation and experimental results match well with each other [see Figs. 5(b)–5(e)], which strongly verifies the nonreciprocal behaviors of our multichannel system.

In our system the gain coefficients at the four giant gain peaks are affected by several experimental parameters, such as the powers of the coupling and probe fields and the temperature of the vapor cell, which makes the gain g quite tunable. Figures 6(a) and 6(b) illustrate that with increasing power P_1 (P_2) of the coupling field 1 (2), the gain curves of all the four weak fields will increase until they finally reach upper limits. This phenomenon reveals a competition between the enhancement process and the saturation effect. The DEIT requires the coupling fields being much stronger than the probe field so as to reduce the absorption of the probe field in the transparency windows, and the FWM processes are

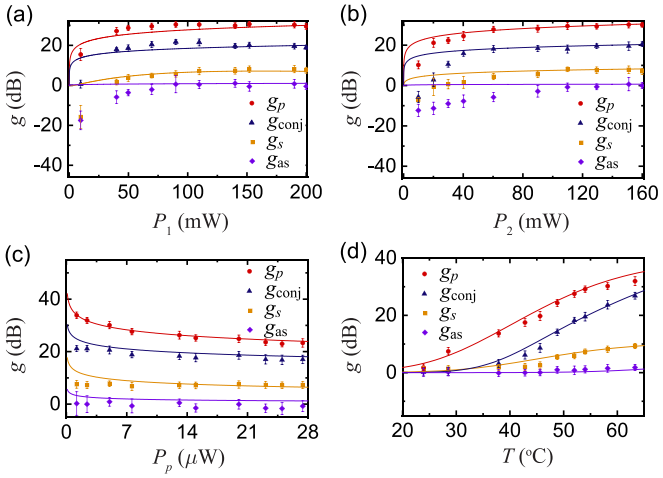

FIG. 6. The dependence of the gain g of the four weak fields on (a) the power P_1 of the coupling field 1, (b) the power P_2 of the coupling field 2, (c) the power P_p of the probe field, and (d) the temperature T of Cs atoms, where $P_2 = 147$ mW, $P_p = 4$ μW, and $T = 55$ °C in (a), $P_1 = 128$ mW, $P_p = 4$ μW, and $T = 55$ °C in (b), $P_1 = 128$ mW, $P_2 = 147$ mW, and $T = 55$ °C in (c), and $P_1 = 128$ mW, $P_2 = 147$ mW, and $P_p = 4$ μW in (d). The red circle dots (probe field), blue triangle dots (conjugated field), orange square dots (Stokes field), and purple diamond dots (anti-Stokes field) denote the experimental results, while the red curves (probe field), blue curves (conjugated field), orange curves (Stokes field), and purple curves (anti-Stokes field) are the theoretical results obtained using Eq. (6). Here, each experimental dot is obtained by averaging 20 sets of measurement data, which are measured under the same experimental conditions. Also, the theoretical values of the gain g of the four weak fields are obtained at $\Delta_p/2\pi = -0.002$, 0.0397, 9.1963, and 9.24 GHz, respectively.

also proportional to the strength of the coupling fields as well. Thus the increasing powers of coupling fields are beneficial to the amplification process. However, the gain coefficients cannot grow indefinitely because of the limited atomic density and the distortion of dispersion curves in high-power region. On the other hand, increasing the power of the probe field, equivalent to decreasing the power of the coupling field, will reduce the four gain rates [cf. Fig. 6(c)]. Even for the ultralow power of the probe field (~ 1 μW), high gain rates can also be obtained. The corresponding theoretical simulations [see solid curves in Figs. 6(a)–6(c)] agree well with the experimental results, besides the difference in the regions of the low powers of two coupling fields [see the regions $P_1 < 50$ mW in Fig. 6(a) and $P_2 < 50$ mW in Fig. 6(b)]. We attribute the discrepancy at lower power to the destruction of FWMs and two DEIT structures [cf. Figs. 2(a)–2(d)]. When one of the coupling fields is too weak, the population distribution shown in Fig. 1(c) and the simplified structures shown in Fig. 2 will be destroyed, on which the theoretical results are based. To be specific, we can take a weak-coupling field 2 as an example. For a very-weak-coupling field 2, the population in $|b_{m_F}\rangle$ is 1/9 for $m_F = -4, -3, \ldots, 4$, while the population in $|a_{m_F}\rangle$ is zero for $m_F = -3, -2, \ldots, 3$. In this case the FWM shown in Fig. 2(c) and the DEIT structures shown in Fig. 2(d) will be destroyed, and the theoretical model becomes invalid.

In addition, the four gain coefficients at the giant gain peaks are also sensitive to the temperature. As shown in Fig. 6(d), the measured gain coefficients monotonically increase versus the temperature T and then reach saturation. This is because the population of Cs atoms in ground states, $|b_{\pm 1}\rangle$ and $|a_0\rangle$, increase with the temperature [cf. Fig. 2(e)], which strengthens the nonlinear processes of amplifications. On the other hand, further increasing the temperature will bring in severe absorption and additional decoherence into the system due to inelastic collisions among Cs atoms. When these two effects have a balance, the gain coefficients reach saturation. Due to the limitation of experimental technology, we only measure the gain coefficients in the region 25 °C $\leqslant T \leqslant$ 65 °C. In the higher-temperature region $T >$ 65 °C, the adverse effects induced by inelastic collisions rather than the population of Cs atoms dominate the nonlinear processes of amplifications. The result may be that with the increasing temperature of Cs atoms, the gain coefficients at the four giant gain peaks decrease [51]. Also, we numerically simulate the theoretical results using Eq. (6) [see solid curves in Fig. 6(d)], which fit the experimental results well.

IV. DISCUSSION AND CONCLUSIONS

Due to the good adjustability of multiple parameters, the group velocities of the four weak fields can be matched well in our system, i.e., $v_g(\omega_p) = v_g(\omega_{\rm conj}) = v_g(\omega_s) = v_g(\omega_{\rm as})$, which is essential for engineering correlated photon pairs [59]. Here the group velocity $v_g(\omega)$ of the optical field can be expressed as

$$v_g(\omega) = \frac{c}{n(\omega) + \omega \frac{\partial}{\partial \omega} n(\omega)}, \tag{7}$$

where c is the velocity of light, and $n(\omega) = 1 + {\rm Re}[\chi(\omega)]$ is the corresponding refractive index. Because the frequencies of the four weak fields are all around the resonance frequency ω_0 of the D1 line, we can take an approximation $\omega \frac{\partial}{\partial \omega} n(\omega) \approx \omega_0 \frac{\partial}{\partial \omega} n(\omega)$, i.e.,

$$v_g(\omega) \approx \frac{c}{1 + {\rm Re}[\chi(\omega)] + \omega_0 \frac{\partial}{\partial \omega} {\rm Re}[\chi(\omega)]}. \tag{8}$$

By numerically analyzing the susceptibility $\chi(\omega)$ in Eq. (3), we find that the slope $\frac{\partial}{\partial \omega} {\rm Re}[\chi(\omega)]$ of the susceptibility at the frequencies of the four weak fields are approximatively equal when the two Rabi frequencies of coupling fields are chosen to be equal, as is shown in Fig. 7(a). For the forward probe field, ${\rm Re}[\chi(\omega_p)] = {\rm Re}[\chi(\omega_{\rm conj})] = {\rm Re}[\chi(\omega_s)] = {\rm Re}[\chi(\omega_{\rm as})] = 0$, which indicates the group velocity matching of the four weak fields, cf. Fig. 7(b). The group velocity matching is an essential requirement for multiwave mixing processes and manipulating the two-bit gates in quantum computation [3,48,60,61], which increases the time of the nonlinear interaction process [62] but also improves the optical storage.

In summary, we have studied the multichannel nonreciprocal amplifications in thermal Cs atoms. Both theoretically and experimentally, four tunable amplification peaks are observed for the forward probe field, while all gain peaks cease to exist in the backward case. With polarizations carefully chosen, the system significantly reduces the spontaneous

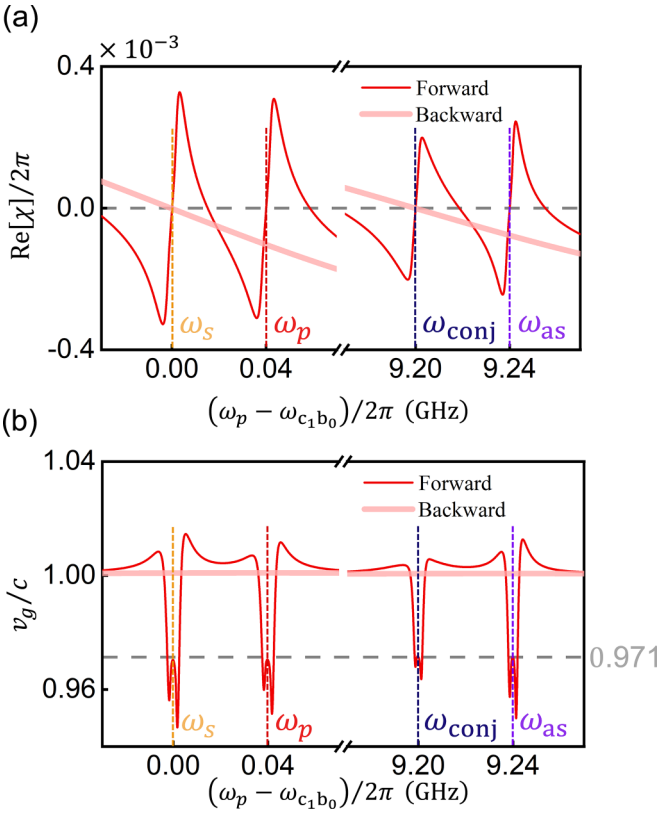

FIG. 7. (a) The real part Re[χ] of the susceptibility using Eq. (3) and (b) the group velocity v_g/c using Eq. (7) in both forward (dark red) and backward (pale red) cases. The group velocity of all the four fields equals to 0.971c, which indicates that the group velocity matching condition is achieved. The Rabi frequencies of the two coupling fields are chosen to be $\Omega_1 = \Omega_2 = 12\ \gamma_{c_0}$, and other parameters are the same as in Fig. 3.

emission noise and thus enhances the signal-to-noise ratio. In addition, the whole setup is all optical, making it easily compatible to miniaturization and integration onto a chip. The adjustability of the gain coefficients makes our system tunable to achieve abundant prospective applications, such as frequency division multiplexing [63] and anti-parity-time-symmetric systems with amplification [64].

ACKNOWLEDGMENTS

We thank J. Q. You and J. X. Zhang for useful discussions.

APPENDIX A: OPTIMAL ANGLES BETWEEN COUPLING FIELDS AND PROBE FIELD

To achieve the four-channel amplifications, the phase-matching conditions of the two FWMs in Figs. 2(a) and 2(c) are required (cf. Fig. 8). For the two FWMs, the scalar phase mismatches in the z direction are denoted as [65]

$$\begin{aligned}\Delta k^{(1)}_{\rm FWM} &= (\omega_1\cos\theta_1 + \omega_2\cos\theta_2 - \omega_p - \omega_{\rm conj})/c \\ &\quad + (\mathrm{Re}[\chi_p]\omega_p + \mathrm{Re}[\chi_{\rm conj}]\omega_{\rm conj})/c, \\ \Delta k^{(2)}_{\rm FWM} &= (\omega_1\cos\theta_1 + \omega_2\cos\theta_2 - \omega_s - \omega_{\rm as})/c \\ &\quad + (\mathrm{Re}[\chi_s]\omega_s + \mathrm{Re}[\chi_{\rm as}]\omega_{\rm as})/c. \end{aligned} \tag{A1}$$

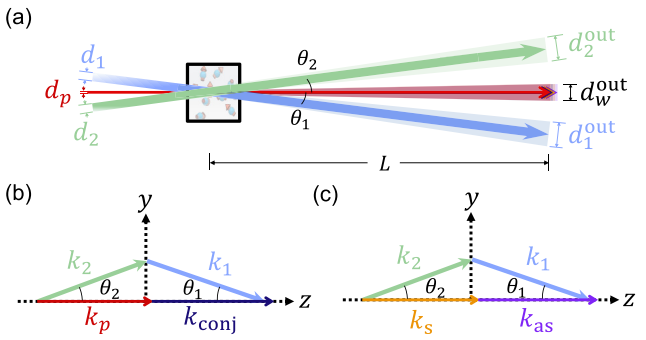

FIG. 8. (a) Schematic diagram of relative angles between coupling fields and probe field. Here the blue arrow (green arrow, red arrow) denotes the coupling field 1 (coupling field 2, probe field), $\theta_{1(2)}$ is the angle between the coupling field 1 (2) and the probe field, L represents the distance between the vapor cell and the detector, and $\{d_1, d_2, d_p\}$ and $\{d_1^{\rm out}, d_2^{\rm out}, d_w^{\rm out}\}$ denote the diameters of the incident beams and the outgoing beams, respectively. Note that the diameters of the four outgoing weak beams are almost the same. (b) and (c) The phase-matching conditions for the two FWMs in Figs. 2(a) and 2(c), respectively.

In the forward case, $\mathrm{Re}[\chi_s] = \mathrm{Re}[\chi_p] = \mathrm{Re}[\chi_{\rm conj}] = \mathrm{Re}[\chi_{\rm as}] = 0$ due to the DEIT structures [see Fig. 7(a)]. Now, the two phase mismatches in Eq. (A1) are reduced to

$$\begin{aligned}\Delta k^{(1)}_{\rm FWM} &= k_1\cos\theta_1 + k_2\cos\theta_2 - k_p - k_{\rm conj}, \\ \Delta k^{(2)}_{\rm FWM} &= k_1\cos\theta_1 + k_2\cos\theta_2 - k_s - k_{\rm as}, \end{aligned} \tag{A2}$$

where the four wave vectors satisfy $k_1 + k_2 = k_p + k_{\rm conj}$ and $k_1 + k_2 = k_s + k_{\rm as}$, i.e., $\omega_1 + \omega_2 = \omega_p + \omega_{\rm conj}$ and $\omega_1 + \omega_2 = \omega_s + \omega_{\rm as}$ guaranteed by the energy conservation in the two FWMs. By solving the phase-matching conditions $\Delta k^{(1)}_{\rm FWM} = \Delta k^{(2)}_{\rm FWM} = 0$, we obtain $\theta_1 = \theta_2 = 0$. This means that the two coupling fields and the probe field need to be collinearly incident.

However, if the two coupling fields and the probe field are collinearly incident, the outgoing coupling fields and the four outgoing weak fields will be mixed. In this case, even using polarizing beam splitters and filters, we cannot distinguish the outgoing coupling fields and the four outgoing weak fields in the experiment, because the frequency of coupling field 1 (coupling field 2) is close to the frequencies of the Stokes and probe fields (anti-Stokes and conjugated fields). Therefore the coupling fields and the probe field are noncollinear in the experiment (corresponding to $\theta_1 \neq 0$ and $\theta_2 \neq 0$), cf. Fig. 8(a). In order to distinguish the outgoing coupling fields and the four outgoing weak fields, the angles θ_1 and θ_2, the distance L between the vapor cell and the detector, the diameters $d_1^{\rm out}$ and $d_2^{\rm out}$ ($d_w^{\rm out}$) of the outgoing coupling fields (outgoing weak fields) should satisfy $L\sin\theta_1 \approx L\theta_1 \geqslant (d_1^{\rm out} + d_w^{\rm out})/2$ and $L\sin\theta_2 \approx L\theta_2 \geqslant (d_2^{\rm out} + d_w^{\rm out})/2$, i.e., $\theta_1 \geqslant (d_1^{\rm out} + d_w^{\rm out})/2L$ and $\theta_2 \geqslant (d_2^{\rm out} + d_w^{\rm out})/2L$. In addition, to meet the scalar phase match in the y direction, the angles θ_1 and θ_2 should satisfy the constraint $\theta_1 \approx \theta_2$. With our experimental conditions, when $\theta_1 = \theta_2 \geqslant 3.45$ mrad, the outgoing coupling fields and the four outgoing weak fields can be distinguished. Taking into account the phase matches, we choose $\theta_1 = \theta_2 = 3.45$ mrad in our experiment. Compared with the case of

$\theta_1 = \theta_2 = 0$, the nonzero angles between coupling fields and probe field (i.e., phase mismatches) slightly shift the locations of the four giant gain peaks as well as slightly weaken the amplification effect in the experiment.

APPENDIX B: STEADY-STATE POPULATION OF Cs ATOMS

The Cs atoms have many sublevels in D1 line, which makes it difficult to analyze amplification processes. In our experiment, by skillfully choosing the polarizations of the coupling fields and using the forbidden nature of the transition $|b_0\rangle \to |c_0\rangle$, almost all Cs atoms are in the ground state $|b_0\rangle$ due to the optical pumping induced by coupling fields [cf. Figs. 1(c) and 2(e)]. Therefore we can only focus on the simplified level diagrams in Figs. 2(a)–2(d).

At low temperature (e.g., $T = 25$ °C), the populations of Cs atoms in other ground states (excluding the state $|b_0\rangle$) are negligible. Now the two FWMs shown in Figs. 2(a) and 2(c) are very weak, and only four transparency windows exist in the gain spectra [cf. Fig. 3(a)]. With the increase of the temperature T of Cs vapor, the population of Cs atoms will be transferred from the ground state $|b_0\rangle$ to the ground states $|b_1\rangle$ and $|a_0\rangle$. When the population of Cs atoms in $|b_1\rangle$ and $|a_0\rangle$ cannot be ignored at, e.g., $T = 43$ °C, the two FWMs shown in Figs. 2(a) and 2(c) become strong, and the four transparency windows in the gain spectra become four gain peaks [cf. Fig. 3(b)]. Further increasing the temperature T of Cs vapor, the populations of Cs atoms in $|b_1\rangle$ and $|a_0\rangle$ increase, and the amplification effect is more significant. In addition, the populations of Cs atoms in $|b_1\rangle$ and $|a_0\rangle$ will also be transferred to $|b_2\rangle$ and $|a_1\rangle$. This can produce other multiwave mixing processes [e.g., the two FWMs shown in Figs. 9(a) and 9(b)], which may enhance the giant gain peaks investigated in the main text or give rise to additional gain peaks in transmission spectra [see Figs. 5(b) and 5(c) and related discussions]. However, since the ratios $\rho_{b_1b_1}/\rho_{b_2b_2}$ (≈ 3) and $\rho_{a_0a_0}/\rho_{a_1a_1}$ (≈ 6.2) are almost constant in the region 20 °C $< T <$ 70 °C [cf. Fig. 9(c)], other multiwave mixing processes induced by the populations of Cs atoms in $|b_2\rangle$ and $|a_1\rangle$ are always much weaker than the two FWMs shown in Figs. 2(a) and 2(c). Therefore our theoretical model only including the two FWMs is reasonable and can describe experimental results well.

APPENDIX C: THE HAMILTONIAN AND THE MASTER EQUATION OF Cs ATOMS

As schematically depicted in Fig. 1, we construct a nonreciprocal optical system using a thermal Cs atomic ensemble in the D1 line, where a probe laser (with frequency ω_p and wave vector k_p) is scanned around the transition $6^2S_{1/2}(F_g = 4) \to 6^2P_{1/2}(F_e = 4)$, a coupling laser (with frequency ω_1 and wave vector k_1) is on-resonance with the transition $6^2S_{1/2}(F_g = 3) \to 6^2P_{1/2}(F_e = 4)$, and another coupling laser (with frequency ω_2 and wave vector k_2) is blue detuned from the transition $6^2S_{1/2}(F_g = 4) \to 6^2P_{1/2}(F_e = 4)$. For convenience, the states $6^2S_{1/2}(F_g = 3, F_g = 4)$ and $6^2P_{1/2}(F_e = 4)$ are denoted as $|a_{m_F}\rangle$, $|b_{m_F}\rangle$, and $|c_{m_F}\rangle$, where m_F is the projection of $F_{g,e}$ along the quantization axis. With the quantization axis chosen, the two horizonal linear polarized (π - polarized)

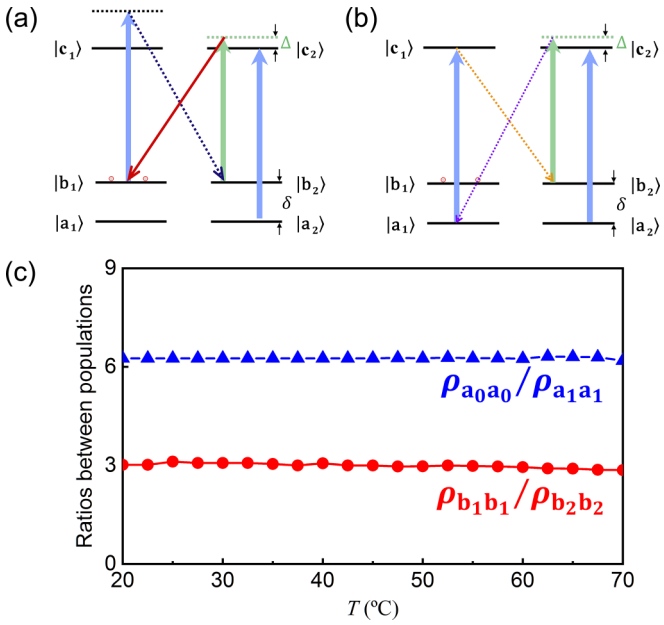

FIG. 9. (a) and (b) The FWM processes relate to ground states $\{|b_1\rangle, |b_2\rangle\}$ and $\{|a_1\rangle, |b_2\rangle\}$, respectively. (c) The ratios between populations, $\rho_{b_1b_1}/\rho_{b_2b_2}$ and $\rho_{a_0a_0}/\rho_{a_1a_1}$, vs the temperature T of the atomic vapor cell, which are calculated using Eqs. (C5)–(C9). The parameters used in the numerical simulation are the same as in Fig. 2(e).

coupling fields and one vertical linear polarized (σ^+- and σ^-- polarized with equal components) probe field interact efficiently with the Cs atoms in the Zeeman sublevels, where the corresponding Rabi frequencies are denoted as $\Omega_{1,2}$ and Ω_p. Now, the total Hamiltonian of the atomic system reads

$$H = H_0 + H_I, \tag{C1}$$

$$H_0 = \sum_{m_F=-3}^{3} \omega_a \sigma_{a_{m_F} a_{m_F}} + \sum_{m_F=-4}^{4} \omega_b \sigma_{b_{m_F} b_{m_F}} + \sum_{m_{F'}=-4}^{4} \omega_c \sigma_{c_{m_{F'}} c_{m_{F'}}}, \tag{C2}$$

$$H_I = \frac{1}{2}\Big[\sum_{m_F=-3}^{3} \Omega_1 e^{i(k_1 z - \omega_1 t)} \sigma_{c_{m_F} a_{m_F}} + \sum_{m_F=-3}^{3} \Omega_2 e^{i(k_2 z - \omega_2 t)} \sigma_{c_{m_F} b_{m_F}} + \text{H.c.} \Big], \tag{C3}$$

where $\sigma_{xy} = |x\rangle\langle y| (\{x, y\} = \{a_{m_F}, b_{m_F}, c_{m_F}\})$ are the operators of Cs atoms, and ω_a (ω_b, ω_c) is the eigenenergy of state $|a_{m_F}\rangle$ ($|b_{m_F}\rangle$, $|c_{m_F}\rangle$). When considering the Doppler effect, the frequencies ω_1 and ω_2 of the two coupling fields in Eq. (C3) become $\omega_1 + k_1 v$ and $\omega_2 + k_2 v$, respectively, where v is the velocity of Cs atoms. In the interaction picture, the Hamiltonian of the system can be converted to

$$H_{\text{int}} = \frac{1}{2}\Big(\sum_{m_F=-3}^{3} \Omega_1 e^{-i\Delta_1 t} \sigma_{c_{m_F} b_{m_F}} + \sum_{m_F=-3}^{3} \Omega_2 e^{-i\Delta_2 t} \sigma_{c_{m_F} b_{m_F}} + \text{H.c.} \Big), \tag{C4}$$

where $\Delta_1 = (\omega_1 + k_1 v) - \omega_{ca}$ is the detuning of coupling field 1 with $\omega_{ca} = \omega_c - \omega_a$, $\Delta_2 = (\omega_2 + k_2 v) - \omega_{cb}$ is the detuning of coupling field 2 with $\omega_{cb} = \omega_c - \omega_b$, and $\Delta_p = \omega_p - \omega_{cb}$ is the detuning of the probe field. With the Hamiltonian of the system in Eq. (C4), we can describe the dynamical evolution of the density matrix elements ρ_{ij} using the master equation [51]:

$$\dot{\rho}_{c_n c_l} = i \sum_{m_F=-4}^{4} \left(\rho_{c_n b_{m_F}} \Omega_{b_{m_F} c_l} - \Omega_{c_n b_{m_F}} \rho_{b_{m_F} c_l}\right) + i \sum_{m_F=-3}^{3} \left(\rho_{c_n a_{m_F}} \Omega_{a_{m_F} c_l} - \Omega_{c_n a_{m_F}} \rho_{a_{m_F} c_l}\right) - \gamma_{c_n c_l} \rho_{c_n c_l}, \tag{C5}$$

$$\dot{\rho}_{b_n b_l} = i \sum_{m_{F'}=-4}^{4} \left(\rho_{b_n c_{m_{F'}}} \Omega_{c_{m_{F'}} b_l} - \Omega_{b_n c_{m_{F'}}} \rho_{c_{m_{F'}} b_l}\right) - \gamma_{b_n b_l} \rho_{b_n b_l} + \delta_{nl} \gamma'_{ab} \sum_{a_j} \rho_{a_j a_j}, \tag{C6}$$

$$\dot{\rho}_{a_n a_l} = i \sum_{m_{F'}=-4}^{4} \left(\rho_{a_n c_{m_{F'}}} \Omega_{c_{m_{F'}} a_l} - \Omega_{a_n c_{m_{F'}}} \rho_{c_{m_{F'}} a_l}\right) - \gamma_{a_n a_l} \rho_{a_n a_l} + \delta_{nl} \gamma'_{ba} \sum_{b_j} \rho_{b_j b_j}, \tag{C7}$$

$$\dot{\rho}_{c_n b_l} = i \sum_{m_{F'}=-4}^{4} \rho_{c_n c_{m_{F'}}} \Omega_{c_{m_{F'}} b_l} - i \sum_{m_F=-4}^{4} \rho_{b_{m_F} b_l} \Omega_{c_n b_{m_F}} + \left(i\Delta_2 - \gamma_{c_n b_l}\right) \rho_{c_n b_l}, \tag{C8}$$

$$\dot{\rho}_{c_n a_l} = i \sum_{m_{F'}=-4}^{4} \rho_{c_n c_{m_{F'}}} \Omega_{c_{m_{F'}} a_l} - i \sum_{m_F=-3}^{3} \rho_{a_{m_F} a_l} \Omega_{c_n a_{m_F}} + \left(i\Delta_1 - \gamma_{c_n a_l}\right) \rho_{c_n a_l}. \tag{C9}$$

Here $\{n, l\}$ are the substitutions of the Zeeman sublevels, $\gamma_{c_n a_l} = \frac{1}{2}(\gamma_{c_n} + \gamma_{a_l})$ is the dephasing rate between $|c_n\rangle$ and $|a_l\rangle$ with the decay rates γ_{c_n} and γ_{a_l}, $\Omega_{c_n a_l (c_n b_l)} = \alpha_{c_n a_l (c_n b_l)} \Omega_{1(2)}$ represents the effective Rabi frequency of coupling field 1 (2) with transition coefficient $\alpha_{c_n a_l (c_n b_l)}$, and the transition of population (ToP) rates γ'_{ab} and γ'_{ba} between $|a\rangle$ and $|b\rangle$ indicate the effects of spin-exchange collisions among Cs atoms [51]. In the considered system, the ToP rates are proportional to the temperature of the Cs atomic vapor cell.

Based on the Runge-Kutta method of orders 4 and 5, we numerically calculating the steady-state populations of the Zeeman sublevels using Eqs. (C5)–(C9) by setting $\dot{\rho}_{ij} = 0$, and the related results are shown in Fig. 2(e) in the main text and Fig. 9(c) in Appendix B. In this numerical simulation, the Doppler effect is ignorable because the propagation directions of two coupling fields are the same.

APPENDIX D: DERIVING THE SUSCEPTIBILITY χ FOR THE WEAK FIELDS

1. The susceptibility χ_1

For the FWM process in Fig. 2(a), the energy levels of Cs atoms can be simplified into five-level structures. In a rotating reference frame with respect to the frequencies of the coupling fields and weak fields, the Hamiltonian of the system can be expressed as

$$H_{\text{eff}}^{(1)} = \Delta_p \sigma_{b_0 b_0} + \Delta_2 \sigma_{b_1 b_1} - (\delta - \Delta_p)\sigma_{c_0 c_0} + \tfrac{1}{2}\left[\Omega_p e^{ik_p z} \sigma_{c_1 b_0} + \Omega_1 e^{ik_1 z}\left(\sigma_{c_1 a_1} + \sigma_{c_0 b_0}\right) + \Omega_2 e^{ik_2 z} \sigma_{c_1 b_1} + \Omega_{\text{conj}} e^{ik_{\text{conj}} z} \sigma_{c_0 b_1} + \text{H.c.}\right], \tag{D1}$$

with $\Delta_p = (\omega_p \pm k_p v) - \omega_{c_1 b_0}$ and $\Delta_{\text{conj}} = (\omega_{\text{conj}} \pm k_{\text{conj}} v) - \omega_{c_1 a_0}$, where Ω_p (Ω_{conj}) is the Rabi frequencies of the probe (conjugated) field, and $+k_p v$ and $+k_{\text{conj}} v$ ($-k_p v$ and $-k_{\text{conj}} v$) correspond to the forward (backward) weak fields. With the above Hamiltonian, the dynamical evolution equations of density matrix elements ρ_{ij} of the system are given by

$$\dot{\rho}_{c_1 b_0} = \dot{\rho}^*_{b_0 c_1} = \frac{i}{2}\left[\Omega_p\left(\rho_{c_1 c_1} - \rho_{b_0 b_0}\right) + \Omega_1\left(\rho_{c_1 c_0} - \rho_{a_1 b_0}\right) - \Omega_2 \rho_{b_1 b_0}\right] + (i\Delta_p - \gamma_{c_1 b_0})\rho_{c_1 b_0}, \tag{D2}$$

$$\dot{\rho}_{a_1 b_0} = \dot{\rho}^*_{b_0 a_1} = \frac{i}{2}\left(\Omega_p \rho_{a_1 c_1} + \Omega_1 \rho_{a_1 c_0} - \Omega_1^* \rho_{c_1 b_0}\right) + \left(i\Delta_p - \gamma_{a_1 b_0}\right)\rho_{a_1 b_0}, \tag{D3}$$

$$\dot{\rho}_{b_1 b_0} = \dot{\rho}^*_{b_0 b_1} = \frac{i}{2}\left(\Omega_p \rho_{b_1 c_1} + \Omega_1 \rho_{b_1 c_0} - \Omega_2^* \rho_{c_1 b_0} - \Omega^*_{\text{conj}} \rho_{c_0 b_0}\right) + \left(i\Delta_{p2} - \gamma_{b_1 b_0}\right)\rho_{b_1 b_0}, \tag{D4}$$

$$\dot{\rho}_{c_1 c_0} = \dot{\rho}^*_{c_0 c_1} = \frac{i}{2}\left(\Omega_1^* \rho_{c_1 b_0} + \Omega^*_{\text{conj}} \rho_{c_1 b_1} - \Omega_p \rho_{b_0 c_0} - \Omega_1 \rho_{a_1 c_0} - \Omega_2 \rho_{b_1 c_0}\right) + \left[i(\delta - \Delta_p) + \gamma_{c_1 c_0}\right]\rho_{c_1 c_0}, \tag{D5}$$

$$\dot{\rho}_{c_1 b_1} = \dot{\rho}^*_{b_1 c_1} = \frac{i}{2}\left[\Omega_2\left(\rho_{c_1 c_1} - \rho_{b_1 b_1}\right) + \Omega_{\text{conj}} \rho_{c_1 c_0} - \Omega_p \rho_{b_0 b_1} - \Omega_1 \rho_{a_1 b_1}\right] + \left(i\Delta_2 - \gamma_{c_1 b_1}\right)\rho_{c_1 b_1}, \tag{D6}$$

$$\dot{\rho}_{c_0 b_0} = \dot{\rho}^*_{b_0 c_0} = \frac{i}{2}\left[\Omega_1\left(\rho_{c_0 c_0} - \rho_{b_0 b_0}\right) + \Omega_p \rho_{c_0 c_1} - \Omega_{\text{conj}} \rho_{b_1 b_0}\right] + \left(i\delta - \gamma_{c_0 b_0}\right)\rho_{c_0 b_0}, \tag{D7}$$

$$\dot{\rho}_{a_1 c_1} = \dot{\rho}^*_{c_1 a_1} = \frac{i}{2}\left[\Omega_1^*\left(\rho_{a_1 a_1} - \rho_{c_1 c_1}\right) + \Omega_p^* \rho_{a_1 b_0} + \Omega_2^* \rho_{a_1 b_1}\right] - \gamma_{a_1 c_1} \rho_{a_1 c_1}, \tag{D8}$$

$$\dot{\rho}_{b_1 c_0} = \dot{\rho}^*_{c_0 b_1} = \frac{i}{2}\left[\Omega^*_{\text{conj}}\left(\rho_{b_1 b_1} - \rho_{c_0 c_0}\right) + \Omega_1^* \rho_{b_1 b_0} - \Omega_2^* \rho_{c_1 c_0}\right] + \left[i(\Delta_{p2} - \delta) - \gamma_{b_1 c_0}\right]\rho_{b_1 c_0}, \tag{D9}$$

$$\dot{\rho}_{b_1 c_1} = \dot{\rho}^*_{c_1 b_1} = \frac{i}{2}\left[\Omega_2^*\left(\rho_{b_1 b_1} - \rho_{c_1 c_1}\right) + \Omega_p^* \rho_{b_1 b_0} + \Omega_1^* \rho_{b_1 a_1} - \Omega^*_{\text{conj}} \rho_{c_0 c_1}\right] - \left(i\Delta_2 + \gamma_{b_1 c_1}\right)\rho_{b_1 c_1}, \tag{D10}$$

$$\dot{\rho}_{a_1 c_0} = \dot{\rho}^*_{c_0 a_1} = \frac{i}{2}\left(\Omega_1^* \rho_{a_1 b_0} + \Omega^*_{\text{conj}} \rho_{a_1 b_1} - \Omega_1^* \rho_{c_1 c_0}\right) - \left[i(\delta - \Delta_p) + \gamma_{a_1 c_0}\right]\rho_{a_1, c_0}, \tag{D11}$$

where $\Delta_{p2} = (\omega_p \pm k_p v) - (\omega_2 + k_2 v)$ denotes the two-photon detuning for the FWM process in Fig. 2(a). In addition, the other two-photon detuning related to this FWM process is $\Delta_{\text{conj1}} = \Delta_{\text{conj}} - \Delta_1 = (\omega_{\text{conj}} \pm k_{\text{conj}} v) - (\omega_1 + k_1 v)$.

To obtain the steady-state solutions of these elements, we take $\dot{\rho}_{ij} = 0$ and keep the nondiagonal elements (i.e., ρ_{ij} with $i \neq j$) up to the first order since we are only interested in the three-order nonlinear process. With the obtained steady state $\rho_{c_1 b_0}$, the susceptibility $\chi_1(v)$ of the weak fields in the group of Cs atoms with velocity v is given by

$$\chi_1(v) = \frac{iN|d_{c_1 b_0}|^2}{\epsilon_0 \Omega_p} \rho_{c_1 b_0}(v), \tag{D12}$$

where N stands for the atomic density, $d_{c_1 b_0} = \langle c_1|\mathbf{d}|b_0\rangle$ is the matric element of the dipole moment $\mathbf{d}$ of Cs atoms, and ϵ_0 denotes the permittivity of free space. In the ensemble of Cs atoms, the velocities of Cs atoms satisfy the Maxwell velocity distribution $f(v) = \exp(-v^2/u^2)/u\sqrt{\pi}$, with $u = \sqrt{2k_B T_{at}/M}$ the most probable velocity, k_B the Boltzmann constant, T_{at} the temperature of atoms, and M the mass of a Cs atom. The susceptibility $\chi_1 = \int_{-\infty}^{\infty} \chi_1(v) f(v) dv$ of the ensemble of Cs atoms reads [48,49,51]

$$\chi_1 = \int_{-\infty}^{\infty} \frac{iN|d_{c_1 b_0}|^2}{\epsilon_0 \Omega_p} \left(C^{(1)}_{\text{DEIT}} + C^{(1)}_{\text{SRS}} + C^{(1)}_{\text{FWM}} e^{i\Delta k^{(1)}_{\text{FWM}} z}\right) \times f(v) dv, \tag{D13}$$

where

$$C^{(1)}_{\text{DEIT}} = \frac{\Omega_p(\bar{\rho}_{b_0 b_0} - \bar{\rho}_{c_1 c_1})}{C_{c_1 b_0}}, \tag{D14}$$

$$C^{(1)}_{\text{SRS}} = \frac{\Omega_p|\Omega_2|^2}{C_{c_1 b_0}} \left[\frac{\bar{\rho}_{a_1 a_1} - \bar{\rho}_{c_1 c_1}}{4i\gamma_{a_1 c_1}(\Delta_p - \gamma_{a_1})} + \frac{\bar{\rho}_{b_1 b_1} - \bar{\rho}_{c_1 c_1}}{2i(\Delta_2 + 2\gamma_{b_1 c_1})(2i\Delta_{p2} - \gamma_{b_1})}\right] - \frac{\Omega_p|\Omega_1|^2}{C_{c_1 b_0}} \frac{\bar{\rho}_{b_0 b_0}}{2[i(\delta - \Delta_p) + \gamma_{c_1 c_0}](2i\delta + \gamma_{c_0})}, \tag{D15}$$

$$C^{(1)}_{\text{FWM}} = \frac{\Omega_1 \Omega^*_{\text{conj}} \Omega_2}{C_{c_1 b_0}} \left\{\frac{\bar{\rho}_{b_1 b_1} - \bar{\rho}_{c_1 c_1}}{4i(\Delta_2 - 2\gamma_{b_1 c_1})[i(\delta - \Delta_p) + \gamma_{c_1 c_0}]} - \frac{\bar{\rho}_{b_0 b_0}}{2i(\Delta_{p2} - \gamma_{b_1})(2i\delta - \gamma_{c_0})}\right\}, \tag{D16}$$

with

$$C_{c_1 b_0} = 2i\Delta_p - \gamma_{c_1} - \frac{|\Omega_1|^2}{2i(\delta - \Delta_p) + 2\gamma_{c_1 c_0}} + \frac{|\Omega_1|^2}{2i\Delta_p - \gamma_{a_1}} + \frac{|\Omega_2|^2}{2i\Delta_{p2} - \gamma_{b_1}}. \tag{D17}$$

In Eq. (4), the first term, C_{DEIT}, denotes the linear part of the susceptibility, while the second and third terms, C_{SRS} and C_{FWM}, are the three-order nonlinear parts of the susceptibility.

2. The susceptibility χ_2

Following similar procedures for χ_1, we then derive the susceptibility χ_2 for the Stokes and anti-Stokes fields. The FWM process in Fig. 2(c) can be described by the following time-independent Hamiltonian,

$$H^{(2)}_{\text{eff}} = \Delta_{\text{as}} \sigma_{a_0 a_0} + \Delta_1 \sigma_{a_1 a_1} + \Delta_2 \sigma_{b_1 b_1} + \tfrac{1}{2}\left[\Omega_{\text{as}} e^{ik_{\text{as}} z} \sigma_{c_1 a_0} + \Omega_2 e^{ik_2 z} \sigma_{c_1 b_1} + \Omega_1 e^{ik_1 z}(\sigma_{c_1 a_1} + \sigma_{c_0 a_0}) + \Omega_s e^{ik_s z} \sigma_{c_0 b_1} + \text{H.c.}\right], \tag{D18}$$

where $\Delta_s = (\omega_s \pm k_s v) - \omega_{c_1 b_0}$, $\Delta_{\text{as}} = (\omega_{\text{as}} \pm k_{\text{conj}} v) - \omega_{c_1 a_0}$, and Ω_s (Ω_{as}) is the Rabi frequency of the Stokes (anti-Stokes) field. From the Hamiltonian (D18), we can derive the dynamical evolution equations of the density matrix elements ρ_{ij}:

$$\dot{\rho}_{c_1 a_0} = \dot{\rho}^*_{a_0 c_1} = \frac{i}{2}\left[\Omega_{\text{as}}(\rho_{c_1 c_1} - \rho_{a_0 a_0}) + \Omega_1(\rho_{c_1 c_0} - \rho_{a_1 a_0}) - \Omega_2 \rho_{b_1 a_0}\right] + (i\Delta_{\text{as}} - \gamma_{c_1 a_0})\rho_{c_1 a_0}, \tag{D19}$$

$$\dot{\rho}_{a_1 a_0} = \dot{\rho}^*_{a_0 a_1} = \frac{i}{2}(\Omega_{\text{as}} \rho_{a_1 c_1} + \Omega_1 \rho_{a_1 c_0} - \Omega^*_1 \rho_{c_1 a_0}) + (i\Delta_{\text{as1}} - \gamma_{a_1 a_0})\rho_{a_1 a_0}, \tag{D20}$$

$$\dot{\rho}_{b_1 a_0} = \dot{\rho}^*_{a_0 b_1} = \frac{i}{2}(\Omega_{\text{as}} \rho_{b_1 c_1} + \Omega_1 \rho_{b_1 c_0} - \Omega^*_2 \rho_{c_1 a_0} - \Omega^*_s \rho_{c_1 a_0}) + (i\Delta_{\text{as2}} - \gamma_{b_1 a_0})\rho_{b_1 a_0}, \tag{D21}$$

$$\dot{\rho}_{c_1 c_0} = \dot{\rho}^*_{c_0 c_1} = \frac{i}{2}(\Omega^*_1 \rho_{c_1 a_0} + \Omega^*_s \rho_{c_1 b_1} - \Omega_{\text{as}} \rho_{a_0 c_0} - \Omega_1 \rho_{a_1 c_0} - \Omega_2 \rho_{b_1 c_0}) + (i\Delta_{\text{as2}} - \gamma_{c_1 c_0})\rho_{c_1 c_0}, \tag{D22}$$

$$\dot{\rho}_{c_1 b_1} = \dot{\rho}^*_{b_1 c_1} = \frac{i}{2}\left[\Omega_2(\rho_{c_1 c_1} - \rho_{b_1 b_1}) + \Omega_s \rho_{c_1 c_0} - \Omega_{\text{as}} \rho_{a_0 b_1} - \Omega_1 \rho_{a_1 b_1}\right] + (i\Delta_2 - \gamma_{c_1 b_1})\rho_{c_1 b_1}, \tag{D23}$$

$$\dot{\rho}_{c_0 a_0} = \dot{\rho}^*_{a_0 c_0} = \frac{i}{2}\left[\Omega_1(\rho_{c_0 c_0} - \rho_{a_0 a_0}) + \Omega_{\text{as}} \rho_{c_0 c_1} - \Omega_s \rho_{b_1 a_0}\right] + (i\Delta_2 - \gamma_{c_0 a_0})\rho_{c_0 a_0}, \tag{D24}$$

$$\dot{\rho}_{a_1 c_1} = \dot{\rho}^*_{c_1 a_1} = \frac{i}{2}\left[\Omega^*_1(\rho_{a_1 a_1} - \rho_{c_1 c_1}) + \Omega^*_p \rho_{a_1 b_0} + \Omega^*_2 \rho_{a_1 b_1}\right] - (i\Delta_1 + \gamma_{a_1 c_1})\rho_{a_1 c_1}, \tag{D25}$$

$$\dot{\rho}_{b_1 c_0} = \dot{\rho}^*_{c_0 b_1} = \frac{i}{2}\left[\Omega^*_s(\rho_{b_1 b_1} - \rho_{c_0 c_0}) + \Omega^*_1 \rho_{b_1 a_0} + \Omega^*_2 \rho_{c_1 c_0}\right] + \left[i(\Delta_{\text{as2}} - \Delta_2) - \gamma_{b_1 c_0}\right]\rho_{b_1 c_0}, \tag{D26}$$

$$\dot{\rho}_{a_1 c_0} = \dot{\rho}^*_{c_0 a_1} = \frac{i}{2}(\Omega^*_1 \rho_{a_1 a_0} + \Omega^*_s \rho_{a_1 b_1} - \Omega^*_1 \rho_{c_1 c_0}) + \left[i(\Delta_{\text{as2}} - \Delta_1) - \gamma_{a_1 c_0}\right]\rho_{a_1 c_0}, \tag{D27}$$

where $\Delta_{\text{as2}} = (\omega_{\text{as}} \pm k_{\text{as}} v) - (\omega_2 + \delta + k_2 v)$ is the two-photon detuning for the FWM process in Fig. 2(c). In addition, the other two-photon detuning in this FWM process can

be expressed as $\Delta_{s1} = \Delta_s - \Delta_1 = (\omega_s + \delta \pm k_s v) - (\omega_1 + k_1 v)$. By solving the above equations with $\dot{\rho}_{ij} = 0$, we can obtain the expression of the susceptibility χ_2 [48,49,51]:

$$\chi_2 = \int_{-\infty}^{\infty} \frac{iN|d_{c_1a_0}|^2}{\epsilon_0 \Omega_{as}} \left(C^{(2)}_{DEIT} + C^{(2)}_{SRS} + C^{(2)}_{FWM} e^{i\Delta k^{(2)}_{FWM} z}\right) \times f(v) dv, \tag{D28}$$

where

$$C^{(2)}_{DEIT} = \frac{\Omega_{as}\left(\bar{\rho}_{a_0a_0} - \bar{\rho}_{c_1c_1}\right)}{C_{c_1a_0}}, \tag{D29}$$

$$C^{(2)}_{SRS} = \frac{\Omega_{as}|\Omega_1|^2}{C_{c_1a_0}} \left[\frac{\bar{\rho}_{a_1a_1} - \bar{\rho}_{c_1c_1}}{\left(2i\Delta_{as1} - \gamma_{a_1}\right)\left(2i\Delta_1 + 2\gamma_{a_1c_1}\right)} + \frac{\bar{\rho}_{a_0a_0}}{(2i\Delta_{as2} - 2\gamma_{c_1c_0})(2i\Delta_2 + \gamma_{c_0})} \right] + \frac{\Omega_{as}|\Omega_2|^2}{C_{c_1a_0}} \frac{\bar{\rho}_{b_1b_1} - \bar{\rho}_{c_1c_1}}{\left(2i\Delta_{as2} - \gamma_{b_1}\right)\left(2i\Delta_2 + 2\gamma_{c_1b_1}\right)}, \tag{D30}$$

$$C^{(2)}_{FWM} = \frac{\Omega_1 \Omega_s^* \Omega_2}{C_{c_1a_0}} \left[\frac{\bar{\rho}_{c_1c_1} - \bar{\rho}_{b_1b_1}}{\left(2i\Delta_{as2} - 2\gamma_{c_1c_0}\right)\left(2i\Delta_2 - 2\gamma_{c_1b_1}\right)} - \frac{\bar{\rho}_{a_0a_0}}{\left(2i\Delta_{as2} - \gamma_{b_1}\right)\left(2i\Delta_2 - \gamma_{c_0}\right)} \right], \tag{D31}$$

with

$$C_{c_1a_0} = 2i\Delta_{as} - \gamma_{c_1} + \frac{|\Omega_1|^2}{2i\Delta_{as2} - 2\gamma_{c_1c_0}} + \frac{|\Omega_1|^2}{2i\Delta_{as2} - \gamma_{b_1}} + \frac{|\Omega_2|^2}{2i\Delta_{as1} - \gamma_{b_1}}. \tag{D32}$$

Here $d_{c_1a_0} = \langle c_1|\mathbf{d}|a_0\rangle$ is the matric element of the dipole moment $\mathbf{d}$.

[1] C. Caloz, A. Alù, S. Tretyakov, D. Sounas, K. Achouri, and Z.-L. Deck-Léger, Electromagnetic Nonreciprocity, Phys. Rev. Appl. **10**, 047001 (2018).

[2] D. Jalas, A. Petrov, M. Eich, W. Freude, S. H. Fan, Z. F. Yu, R. Baets, M. Popovic, A. Melloni, J. D. Joannopoulos, M. Vanwolleghem, C. R. Doerr, and H. Renner, What is–and what is not–an optical isolator, Nat. Photonics **7**, 579 (2013).

[3] L. Fan, J. Wang, L. T. Varghese, H. Shen, B. Niu, Y. Xuan, A. M. Weiner, and M. H. Qi, An all-silicon passive optical diode, Science **335**, 447 (2012).

[4] Y. Wang, W. Xiong, Z. Xu, G. Q. Zhang, and J. Q. You, Dissipation-induced nonreciprocal magnon blockade in a magnon-based hybrid system, Sci. China Phys. Mech. Astron. **65**, 260314 (2022).

[5] A. B. Khanikaev and A. Alu, Optical isolators nonlinear dynamic reciprocity, Nat. Photonics **9**, 359 (2015).

[6] P. Lodahl, S. Mahmoodian, S. Stobbe, A. Rauschenbeutel, P. Schneeweiss, J. Volz, H. Pichler, and P. Zoller, Chiral quantum optics, Nature (London) **541**, 473 (2017).

[7] R. J. Potton, Reciprocity in optics, Rep. Prog. Phys. **67**, 717 (2004).

[8] J. Y. Chin, T. Steinle, T. Wehlus, D. Dregely, T. Weiss, V. I. Belotelov, B. Stritzker, and H. Giessen, Nonreciprocal plasmonics enables giant enhancement of thin-film Faraday rotation, Nat. Commun. **4**, 1599 (2013).

[9] Z. F. Yu and S. H. Fan, Complete optical isolation created by indirect interband photonic transitions, Nat. Photonics **3**, 303 (2009).

[10] T. Ozawa, H. M. Price, A. Amo, N. Goldman, M. Hafezi, L. Lu, M. C. Rechtsman, D. Schuster, J. Simon, O. Zilberberg, and I. Carusotto, Topological photonics, Rev. Mod. Phys. **91**, 015006 (2019).

[11] D. L. Sounas and A. Alu, Non-reciprocal photonics based on time modulation, Nat. Photonics **11**, 774 (2017).

[12] T. Dinc, M. Tymchenko, A. Nagulu, D. Sounas, A. Alu, and H. Krishnaswamy, Synchronized conductivity modulation to realize broadband lossless magnetic-free non-reciprocity, Nat. Commun. **8**, 795 (2017).

[13] N. A. Estep, D. L. Sounas, J. Soric, and A. Alu, Magnetic-free non-reciprocity and isolation based on parametrically modulated coupled-resonator loops, Nat. Phys. **10**, 923 (2014).

[14] E. Galiffi, P. A. Huidobro, and J. B. Pendry, Broadband Nonreciprocal Amplification in Luminal Metamaterials, Phys. Rev. Lett. **123**, 206101 (2019).

[15] X. P. Zhou, S. K. Gupta, X. Y. Zhu, G. X. Su, P. Zhan, Y. M. Liu, Z. Chen, M. H. Lu, and Z. L. Wang, Nonreciprocal Isolation and Wavelength Conversion via a Spatiotemporally Engineered Cascaded Cavity, Phys. Rev. Appl. **13**, 044037 (2020).

[16] L. M. de Lepinay, E. Damskagg, C. F. Ockeloen-Korppi, and M. A. Sillanpaa, Realization of Directional Amplification in a Microwave Optomechanical Device, Phys. Rev. Appl. **11**, 034027 (2019).

[17] M. A. Miri, F. Ruesink, E. Verhagen, and A. Alu, Optical Nonreciprocity Based on Optomechanical Coupling, Phys. Rev. Appl. **7**, 064014 (2017)

[18] A. Metelmann and A. A. Clerk, Nonreciprocal Photon Transmission and Amplification via Reservoir Engineering, Phys. Rev. X **5**, 021025 (2015).

[19] K. J. Fang, J. Luo, A. Metelmann, M. H. Matheny, F. Marquardt, A. A. Clerk, and O. Painter, Generalized nonreciprocity in an optomechanical circuit via synthetic magnetism and reservoir engineering, Nat. Phys. **13**, 465 (2017).

[20] E. A. Kittlaus, P. O. Weigel, and W. M. Jones, Low-loss nonlinear optical isolators in silicon, Nat. Photonics **14**, 338 (2020).

[21] A. M. Mahmoud, A. R. Davoyan, and N. Engheta, All-passive nonreciprocal metastructure, Nat. Commun. **6**, 8359 (2015).

[22] B. Y. Jin and C. Argyropoulos, Self-Induced Passive Nonreciprocal Transmission by Nonlinear Bifacial Dielectric Metasurfaces, Phys. Rev. Appl. **13**, 054056 (2020).

[23] N. Bender, S. Factor, J. D. Bodyfelt, H. Ramezani, D. N. Christodoulides, F. M. Ellis, and T. Kottos, Observation of Asymmetric Transport in Structures with Active Nonlinearities, Phys. Rev. Lett. **110**, 234101 (2013).

[24] D. W. Wang, H. T. Zhou, M. J. Guo, J. X. Zhang, J. Evers, and S. Y. Zhu, Optical Diode Made from a Moving Photonic Crystal, Phys. Rev. Lett. **110**, 093901 (2013).

[25] W. Gou, T. Chen, D. Z. Xie, T. Xiao, T. S. Deng, B. Gadway, W. Yi, and B. Yan, Tunable Nonreciprocal Quantum Transport through a Dissipative Aharonov-Bohm Ring in Ultracold Atoms, Phys. Rev. Lett. **124**, 070402 (2020).

[26] X. W. Xu, Y. Li, B. J. Li, H. Jing, and A. X. Chen, Nonreciprocity via Nonlinearity and Synthetic Magnetism, Phys. Rev. Appl. **13**, 044070 (2020).

[27] P. F. Yang, X. W. Xia, H. He, S. K. Li, X. Han, P. Zhang, G. Li, P. F. Zhang, J. P. Xu, Y. P. Yang, and T. C. Zhang, Realization of Nonlinear Optical Nonreciprocity on a Few-Photon Level Based on Atoms Strongly Coupled to an Asymmetric Cavity, Phys. Rev. Lett. **123**, 233604 (2019).

[28] K. Y. Xia, F. Nori, and M. Xiao, Cavity-Free Optical Isolators and Circulators Using a Chiral Cross-Kerr Nonlinearity, Phys. Rev. Lett. **121**, 203602 (2018).

[29] E. Z. Li, D. S. Ding, Y. C. Yu, M. X. Dong, L. Zeng, W. H. Zhang, Y. H. Ye, H. Z. Wu, Z. H. Zhu, W. Gao, G. C. Guo, and B. S. Shi, Experimental demonstration of cavity-free optical isolators and optical circulators, Phys. Rev. Res. **2**, 033517 (2020).

[30] G. W. Lin, S. C. Zhang, Y. Q. Hu, Y. P. Niu, J. B. Gong, and S. Q. Gong, Nonreciprocal Amplification with Four-Level Hot Atoms, Phys. Rev. Lett. **123**, 033902 (2019).

[31] S. C. Zhang, G. W. Lin, Y. Q. Hu, Y. H. Qi, Y. P. Niu, and S. Q. Gong, Cavity-Free Circulator with Low Insertion Loss Using Hot Atoms, Phys. Rev. Appl. **14**, 024032 (2020).

[32] L. M. Duan, M. D. Lukin, J. I. Cirac, and P. Zoller, Long-distance quantum communication with atomic ensembles and linear optics, Nature (London) **414**, 413 (2001).

[33] P. G. Kwiat, K. Mattle, H. Weinfurter, A. Zeilinger, A. V. Sergienko, and Y. H. Shih, New High-Intensity Source of Polarization-Entangled Photon Pairs, Phys. Rev. Lett. **75**, 4337 (1995).

[34] C. Shu, P. Chen, T. K. A. Chow, L. B. Zhu, Y. H. Xiao, M. M. T. Loy, and S. W. Du, Subnatural-linewidth biphotons from a doppler-broadened hot atomic vapour cell, Nat. Commun. **7**, 12783 (2016).

[35] Y. W. Cho, K. K. Park, J. C. Lee, and Y. H. Kim, Engineering Frequency-Time Quantum Correlation of Narrow-Band Biphotons from Cold Atoms, Phys. Rev. Lett. **113**, 063602 (2014).

[36] A. Zavatta, M. Artoni, and G. La Rocca, Engineering of heralded narrowband color-entangled states, Phys. Rev. A **99**, 031802(R) (2019).

[37] V. Balic, D. A. Braje, P. Kolchin, G. Y. Yin, and S. E. Harris, Generation of Paired Photons with Controllable Waveforms, Phys. Rev. Lett. **94**, 183601 (2005).

[38] K. K. Park, J. H. Kim, T. M. Zhao, Y. W. Cho, and Y. H. Kim, Measuring the frequency-time two-photon wavefunction of narrowband entangled photons from cold atoms via stimulated emission, Optica **4**, 1293 (2017).

[39] J. Park, H. Kim, and H. S. Moon, Polarization-Entangled Photons from a Warm Atomic Ensemble Using a Sagnac Interferometer, Phys. Rev. Lett. **122**, 143601 (2019).

[40] T. M. Zhao, Y. S. Ihn, and Y. H. Kim, Direct Generation of Narrow-Band Hyperentangled Photons, Phys. Rev. Lett. **122**, 123607 (2019).

[41] Q. F. Chen, B. S. Shi, Y. S. Zhang, and G. C. Guo, Entanglement of the orbital angular momentum states of the photon pairs generated in a hot atomic ensemble, Phys. Rev. A **78**, 053810 (2008).

[42] J. H. Wang, J. F. Herrmann, J. D. Witmer, A. H. Safavi-Naeini, and S. H. Fan, Photonic Modal Circulator Using Temporal Refractive-Index Modulation with Spatial Inversion Symmetry, Phys. Rev. Lett. **126**, 193901 (2021).

[43] M. Fleischhauer, A. Imamoglu, and J. P. Marangos, Electromagnetically induced transparency: Optics in coherent media, Rev. Mod. Phys. **77**, 633 (2005).

[44] M. D. Eisaman, A. Andre, F. Massou, M. Fleischhauer, A. S. Zibrov, and M. D. Lukin, Electromagnetically induced transparency with tunable single-photon pulses, Nature (London) **438**, 837 (2005).

[45] S. Y. Hua, J. M. Wen, X. S. Jiang, Q. Hua, L. Jiang, and M. Xiao, Demonstration of a chip-based optical isolator with parametric amplification, Nat. Commun. **7**, 13657 (2016).

[46] C. Q. Wang, X. F. Jiang, G. M. Zhao, M. Z. Zhang, C. W. Hsu, B. Peng, A. D. Stone, L. Jiang, and L. Yang, Electromagnetically induced transparency at a chiral exceptional point, Nat. Phys. **16**, 334 (2020).

[47] Y. Zuo, B. H. Li, Y. J. Zhao, Y. Jiang, Y. C. Chen, P. Chen, G. B. Jo, J. W. Liu, and S. W. Du, All-optical neural network with nonlinear activation functions, Optica **6**, 1132 (2019).

[48] S. Rebic, D. Vitali, C. Ottaviani, P. Tombesi, M. Artoni, F. Cataliotti, and R. Corbalan, Polarization phase gate with a tripod atomic system, Phys. Rev. A **70**, 032317 (2004).

[49] H. M. M. Alotaibi and B. C. Sanders, Double-double electromagnetically induced transparency with amplification, Phys. Rev. A **89**, 021802(R) (2014).

[50] D. A. Steck, Cesium D Line Data, available online at http://steck.us/alkalidata (revision 2.1.4, 23 December 2010).

[51] D. Wang, C. Liu, C. S. Xiao, J. X. Zhang, H. M. M. Alotaibi, B. C. Sanders, L. G. Wang, and S. Y. Zhu, Strong coherent light amplification with double electromagnetically induced transparency coherences, Sci. Rep. **7**, 5796 (2017).

[52] Y. Mei, Y. Zhou, S. Zhang, J. Li, K. Liao, H. Yan, S.-L. Zhu, and S. Du, Einstein-Podolsky-Rosen Energy-Time Entanglement of Narrow-Band Biphotons, Phys. Rev. Lett. **124**, 010509 (2020).

[53] G. Dmochowski, A. Feizpour, M. Hallaji, C. Zhuang, A. Hayat, and A. M. Steinberg, Experimental Demonstration of the Effectiveness of Electromagnetically Induced Transparency for Enhancing Cross-Phase Modulation in the Short-Pulse Regime, Phys. Rev. Lett. **116**, 173002 (2016).

[54] J. L. Everett, G. T. Campbell, Y. W. Cho, P. Vernaz-Gris, D. B. Higginbottom, O. Pinel, N. P. Robins, P. K. Lam, and B. C. Buchler, Dynamical observations of self-stabilizing stationary light, Nat. Phys. **13**, 68 (2017).

[55] K. K. Park, Y. W. Cho, Y. T. Chough, and Y. H. Kim, Experimental Demonstration of Quantum Stationary Light Pulses in an Atomic Ensemble, Phys. Rev. X **8**, 021016 (2018).

[56] C. R. Murray and T. Pohl, Coherent Photon Manipulation in Interacting Atomic Ensembles, Phys. Rev. X **7**, 031007 (2017).

[57] H. R. Hamedi, J. Ruseckas, and G. Juzeliunas, Exchange of optical vortices using an electromagnetically-induced-transparency-based four-wave-mixing setup, Phys. Rev. A **98**, 013840 (2018).

[58] L. Yang, L. Zhang, X. Li, L. Han, G. Fu, N. B. Manson, D. Suter, and C. Wei, Autler-Townes effect in a strongly

driven electromagnetically induced transparency resonance, Phys. Rev. A **72**, 053801 (2005).

[59] M. D. Lukin and A. Imamoglu, Nonlinear Optics and Quantum Entanglement of Ultraslow Single Photons, Phys. Rev. Lett. **84**, 1419 (2000).

[60] L. Deng and M. G. Payne, Inhibiting the Onset of the Three-Photon Destructive Interference in Ultraslow Propagation-Enhanced Four-Wave Mixing with Dual Induced Transparency, Phys. Rev. Lett. **91**, 243902 (2003).

[61] L. Deng and M. G. Payne, Three-photon destructive interference in ultraslow-propagation-enhanced four-wave mixing, Phys. Rev. A **68**, 051801(R) (2003).

[62] M. M. Kash, V. A. Sautenkov, A. S. Zibrov, L. Hollberg, G. R. Welch, M. D. Lukin, Y. Rostovtsev, E. S. Fry, and M. O. Scully, Ultraslow Group Velocity and Enhanced Nonlinear Optical Effects in a Coherently Driven Hot Atomic Gas, Phys. Rev. Lett. **82**, 5229 (1999).

[63] M. Pankratova, A. Vasylchenkova, S. A. Derevyanko, N. B. Chichkov, and J. E. Prilepsky, Signal-Noise Interaction in Optical-Fiber Communication Systems Employing Nonlinear Frequency-Division Multiplexing, Phys. Rev. Appl. **13**, 054021 (2020).

[64] Y. Jiang, Y. Mei, Y. Zuo, Y. Zhai, J. Li, J. Wen, and S. Du, Anti-Parity-Time Symmetric Optical Four-Wave Mixing in Cold Atoms, Phys. Rev. Lett. **123**, 193604 (2019).

[65] H. T. Zhou, D. W. Wang, D. Wang, J. X. Zhang, and S. Y. Zhu, Efficient reflection via four-wave mixing in a Doppler-free electromagnetically-induced-transparency gas system, Phys. Rev. A **84**, 053835 (2011).